

Triangulated Wireframe Structures Assembled Using Single-Stranded DNA Tiles

Michael Matthies,[†] Nayan P. Agarwal,[†] Erik Poppleton,[§] Foram M. Joshi,[†] Petr Šulc,^{*,§,||} and Thorsten L. Schmidt^{*,†,‡,§,||}

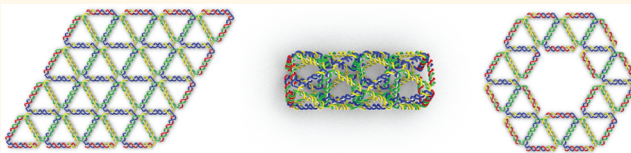
[†]Center for Advancing Electronics Dresden (cfaed), Faculty of Chemistry and Food Chemistry and [‡]B CUBE Center for Molecular Bioengineering, Technische Universität Dresden, 01062 Dresden, Germany

[§]Center for Molecular Design and Biomimetics, The Biodesign Institute, Arizona State University, 1001 South McAllister Avenue, Tempe, Arizona 85281, United States

^{||}School of Molecular Sciences Arizona State University, Physical Sciences Building, Room D-102, PO Box 871604, Tempe, Arizona 85287-1604, United States

Supporting Information

ABSTRACT: The field of structural DNA nanotechnology offers a wide range of design strategies with which to build structures with a desired aspect ratio, size, and shape. Compared with traditional close-packed DNA structures, triangulated wireframe structures require less material per surface or volume unit and improve the stability in biologically relevant conditions due to the reduced electrostatic repulsion. Herein, we expand the design space of the DNA single-stranded tile method to cover a range of anisotropic, finite, triangulated wireframe structures as well as a number of one-dimensional crystalline assemblies. These structures are composed of six-arm junctions with a single double helix as connecting edges that assemble in physiologically relevant salinities. For a reliable folding of the structures, single-stranded spacers 2–4 nucleotides long have to be introduced in the junction connecting neighboring arms. Coarse-grained molecular dynamics simulations using the oxDNA model suggests that the spacers prevent the stacking of DNA helices, thereby facilitating the assembly of planar geometries.



KEYWORDS: structural DNA nanotechnology, single-stranded tiles, triangulated wireframe structures, molecular dynamics simulations

Advances in DNA nanotechnology have paved a reliable bottom-up path for the construction of nanoscale shapes and devices using DNA motifs.^{1–5} DNA structures can be used to arrange a wide variety of materials, allowing the exploration of applications in photonics,^{6–8} biophysics,^{9–11} crystallography,^{12–14} molecular biology,¹⁵ and nanomedicine.¹⁶ The two most common methods of producing addressable 2D and 3D mega-Dalton size structures are DNA origami^{17,18} and single-stranded tiles (SSTs), which, for three-dimensional structures, are also referred to as single-stranded bricks (SSBs).^{19–21} DNA origami structures are folded using a long single-stranded DNA (usually the genome of the M13 bacteriophage) called the “scaffold strand” into the desired shape with the help of short synthetically produced oligonucleotides. The DNA origami method is preferred by many researchers over SST because the structures typically fold very robustly and with greater yields (>90%) than the SST or SSB structures of comparable sizes.²² Moreover, the design process is suitable even for beginners when using the standard computer-aided design tool caDNAno.²³

Nevertheless, SST and SSB structures can have several advantages over DNA origami. There is full control on the

used DNA sequences, and there are no limitations on exploring the interaction motif space of the DNA molecules,²⁴ whereas scaffold sequences are usually biologically determined. The design process of DNA origami can be more complex than for SST or SSB structures because it is necessary to find a suitable scaffold strand routing path throughout the DNA origami structure, which can influence folding pathways and yields.²⁵ Next, many synthetic oligonucleotides are necessary to fold the common and commercially available scaffolds, making the synthesis of full-sized structures expensive, unless enzymatic gap filling is used.²⁶ Finally, when working with commercially available staple strands and scaffold strands, the price of DNA origami structures is dominated by the price of the scaffold strand (Figure S1). For applications that require large-scale synthesis, such as nanomedical applications, scaffold strands can be produced in-house, which reduces costs significantly. Recently, a specialized and laborious procedure was employed to scale up both scaffold and staple strand production to the

Received: October 19, 2018

Accepted: January 9, 2019

Published: January 9, 2019

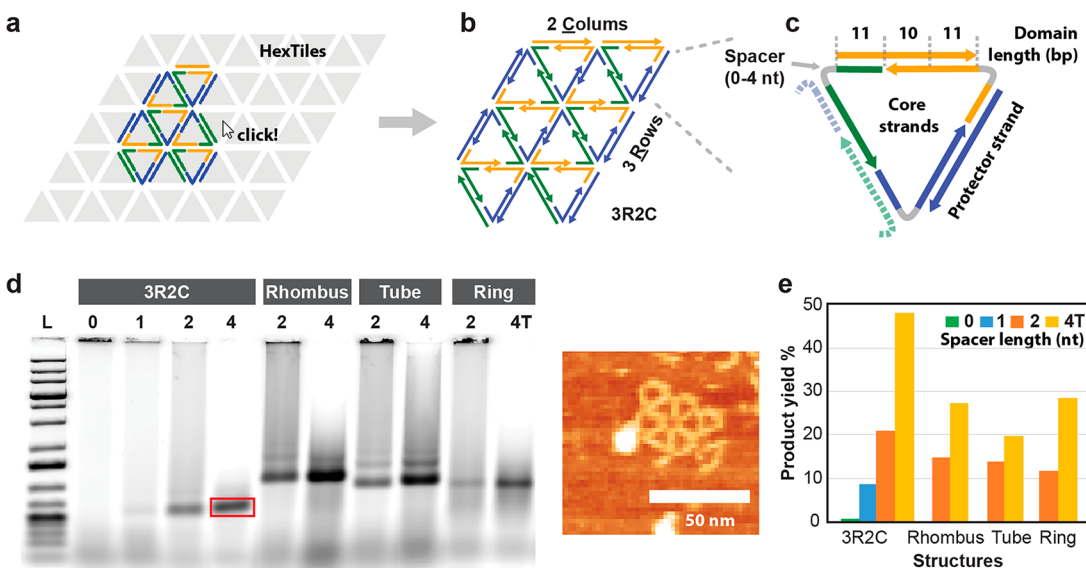


Figure 1. Design pipeline, nomenclature, and product yield estimation of triangulated single-stranded tile structures. (a) A representative test structure is constructed and reproduced on the virtual canvas of the computer-aided design tool called “Hex-Tiles” (Figure S2). (b) The name of the structures is decided by the number of rows and columns that constitute them. In the example, the structure is called “3R2C” because it is composed of three rows and two columns. (c) The oligonucleotides that make up the triangle have 3 interacting domains of 11, 11, and 10 nt, respectively, as well as a variable-length spacer (either 0, 1, 2, or 4 nt). (d) Agarose gel electrophoresis results of four test structures: 3R2C, a rhombus, a tube and a ring (compare Figure 3) with different spacer lengths. The atomic force microscopy (AFM) micrograph to the right shows the 4 nt spacer version of 3R2C extracted from the red rectangular region marked on the gel. Scale bar: 50 nm. (e) Product yields were determined for all the different structures using ImageJ software.

gram scale with biotechnological methods.²⁷ For many laboratories it is, however, more cost- and time-efficient to purchase scaffolds.

SST structures, however can be scaled up easily with hundreds to thousands of chemically synthesized components, without a scaffold from a biological source.²⁸ This also enables the utilization of chemically modified strands for tracking and stabilization.^{29–31} Such modified DNA structures can be exposed to biologically relevant conditions for longer times than the conventional DNA origami structures without employing additional protective strategies.^{32–34} Another advantage of SST and SSB designs is the ease of designing infinite, crystalline structures.^{19,35}

This feature was utilized to study the biophysical properties of DNA structures³⁶ as well as for the construction of accurate model systems to study semiflexible polymer networks.^{37,38} It has also been shown that these structures can be used to mimic biologically relevant propulsion mechanisms such as flagella.³⁹

Traditional DNA origami, SST, and SSB structures rely on the compact arrangement of parallel “solid” DNA double helices on either a square or a hexagonal lattice.⁴⁰ More recently, wireframe structures consisting of a hollow mesh of geometric primitives are gaining interest.^{41–48} This construction principle decreases the material to volume ratio compared to a compact lattice-based design. A subset of these DNA origami structures, in which the edges of the mesh consist of a single DNA double helix and the mesh tiling is composed of triangles, has shown robust assembly and increased resistance to low-salt buffers.^{44–46} Another property of these structures is greater structural stability because triangles offer higher intrinsic shear force resistance as opposed to other geometric primitives.⁴² However, this construction principle is not yet adapted for SST designs.

In this manuscript, we have expanded the design space of SST structures to utilize equilateral triangles as the building block. The robustness of this method was demonstrated by the assembly and characterization of four finite structures as well as a number of 1D crystal structures. A mechanism to control the crystal growth was also explored, and a general computer-aided design pipeline for the construction of these structures is presented. Additionally, coarse-grained molecular dynamics simulations were performed to get a deeper insight in the observed structural behavior of the structures.

DESIGNING THE STRUCTURES

For the production of the designs, we have developed “Hex-Tiles” (Figure 1a), a software package specifically designed for the construction of triangulated wireframe SST structures, because existing free-form DNA construction tools such as Tiamat,⁴⁹ Uniquimer3D, or vHelix are either not specifically built for the construction of uniform wireframe lattices with a repeating SST motif or do not offer an elegant way to manage the produced DNA sequences.^{44,50} In HexTiles, the user is presented with a virtual canvas (an imaginary plane, tiled by the motif) on which the desired triangles of a structure are selected with the mouse. Similar to the classical SST,²⁰ two types of oligonucleotides were used in our triangulated SSTs design: core and edge strands (Figure 1b,c). All strands have three domains of 11, 11, and 10 nucleotides (nt), respectively, instead of 4 interacting domains in the widely used SST designs.²⁰ All edges of the triangles consist of 3 helical turns of DNA (32 base pairs).

After the designing process is finished, the program generates the oligonucleotide sequences necessary to form the desired design. The sequences are generated randomly with no constraints. Because typical SST designs require hundreds of oligonucleotides, the program also generates a list

with the distribution of the newly generated sequences across 96-well plates, differentiated between plates containing core strands and edge strands. This information is included in the design file, thus simplifying the ordering and pipetting of the SST structures (discussed in more detail in Figure S2). Existing designs can be easily modified, thus facilitating the reuse of the existing strand sequences.

RESULTS AND DISCUSSION

To test the design pipeline, we designed a test structure consisting of three rows and two columns (3R2C; see Figure S5 for nomenclature) with different spacer lengths (0, 1, 2, and 4 thymidine, T) at the vertices connecting two edges (Figure 1c). We observed that no structures formed in the 0 T case (Figure 1d). This can potentially be attributed to undesired stacking interactions between adjacent DNA helices that form the arms of the six-arm junctions during the assembly process or due to the accumulation of geometric strain.⁵¹ Very little product (<10%) was observed when a spacer of one thymine base was introduced, indicating that even with the introduction of an extra base, the hypothesized stacking or geometric strain are still prominent.

The introduction of a spacer of two or four thymine bases resulted in the formation of the desired product with an improved yield (~20% and ~50% of the total lane intensity; Figure 1e). Increasing the spacer length further is unlikely to increase yields significantly because hardly any aggregates that limit the folding yields were visible in the gels anymore for the 4 nt spacer structures (Figure 1d). Furthermore, longer spacers would render the structures overly flexible, which reduces their potential to precisely position functional elements.

The correctly assembled structures were also visible on the atomic force microscopy (AFM) micrographs (Figures 1d inset and S6). The best synthesis yields were observed for a spacer length of 4 nt (48%; Figure 1e), and we hypothesized that an increased spacer length effectively prevents stacking and offers more conformational freedom, facilitating the product assembly. To gain further insights into the conformations adopted by the 6-arm junctions that comprise the 3R2C structures, we performed molecular dynamics simulations with the oxDNA model,^{52–54} a coarse-grained model that represents each nucleotide as a single particle with multiple interaction sites. The model is parametrized to reproduce mechanical, structural, and thermodynamic properties of DNA and has been successfully applied to a wide range of systems in DNA biophysics and nanotechnology. Where available, quantitative agreement with experimental measurements was obtained.^{55–57}

We simulated junctions with varying spacer lengths from 0 to 4 thymidines. We observed qualitatively different behaviors for the 6-arm junctions with a 0 nt spacer compared with the junctions with 1 nt or longer spacer. Typical configurations of simulated junctions with a 0 nt spacer are shown in Figures 2a and S4a. The arms of the junction have a preference to form a continuous duplex through base-stacking interactions originating at the junction. The junction itself dynamically switches between different states, in which a given arm preferentially stacks with one of its neighboring arms. This can be seen in the free-energy profile that shows a minimum at around 160 degrees for the neighboring arms (Figure 2a). We also observed that junctions with a 0 nt spacer rarely adopt a planar conformation, with all the arms in the same plane, because that would require breaking of the stacking

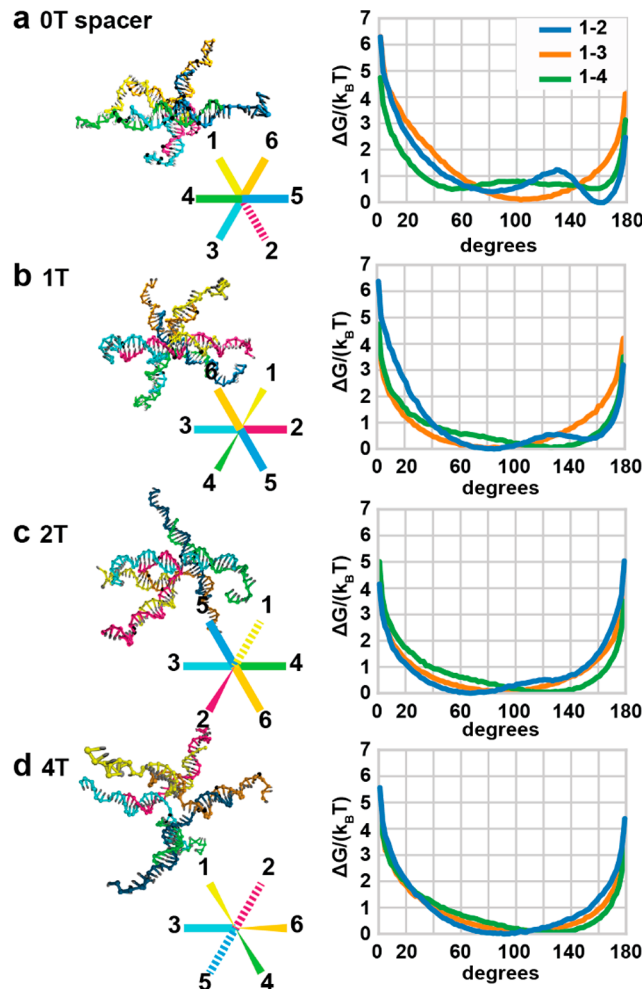


Figure 2. Coarse-grained molecular dynamics simulations using the oxDNA model of the 6-arm junctions with varying spacer lengths from 0 to 4 thymidine (T) bases (see panels a–d). The left column illustrates the snapshots of typical configurations from simulations along with a schematic 2D diagram visualizing the positions of the 6 arms. Solid lines depict arms in the plane, while dashed or pointed lines represent arms out of the plane. For all junction variants, simulations of 11 μ s duration were performed (see Figure S3 and trajectory animations 1–4 for example trajectories), and 40 replicas were run per junction. The right column shows the free-energy landscape (obtained by Boltzmann inversion) as a function of angle between the different pairs of arms depicted in the 2D diagram (the reference orientation is depicted in Figure S4e) of the junction, thus illustrating the preferred conformation of the arms of the junction. A detailed description of the simulation is provided in the Materials and Methods section.

interactions. This observation would explain the experimental data, in which no 3R2C structures were formed for the 0 nt spacer design.

In contrast, six-arm junctions with 1 nt or longer spacers are more flexible, and we do not observe a stacked conformation linking two neighboring arms. However, the angles between selected pairs of junction arms are correlated, with a preference for angles of 60 and 160 degrees between next-nearest neighbors and 140 degrees with the opposite arm for the 1 nt spacer junction (Figure 2b).

Even though the alternative conformations of the six-arm junctions are separated by only a small difference in the ΔG in

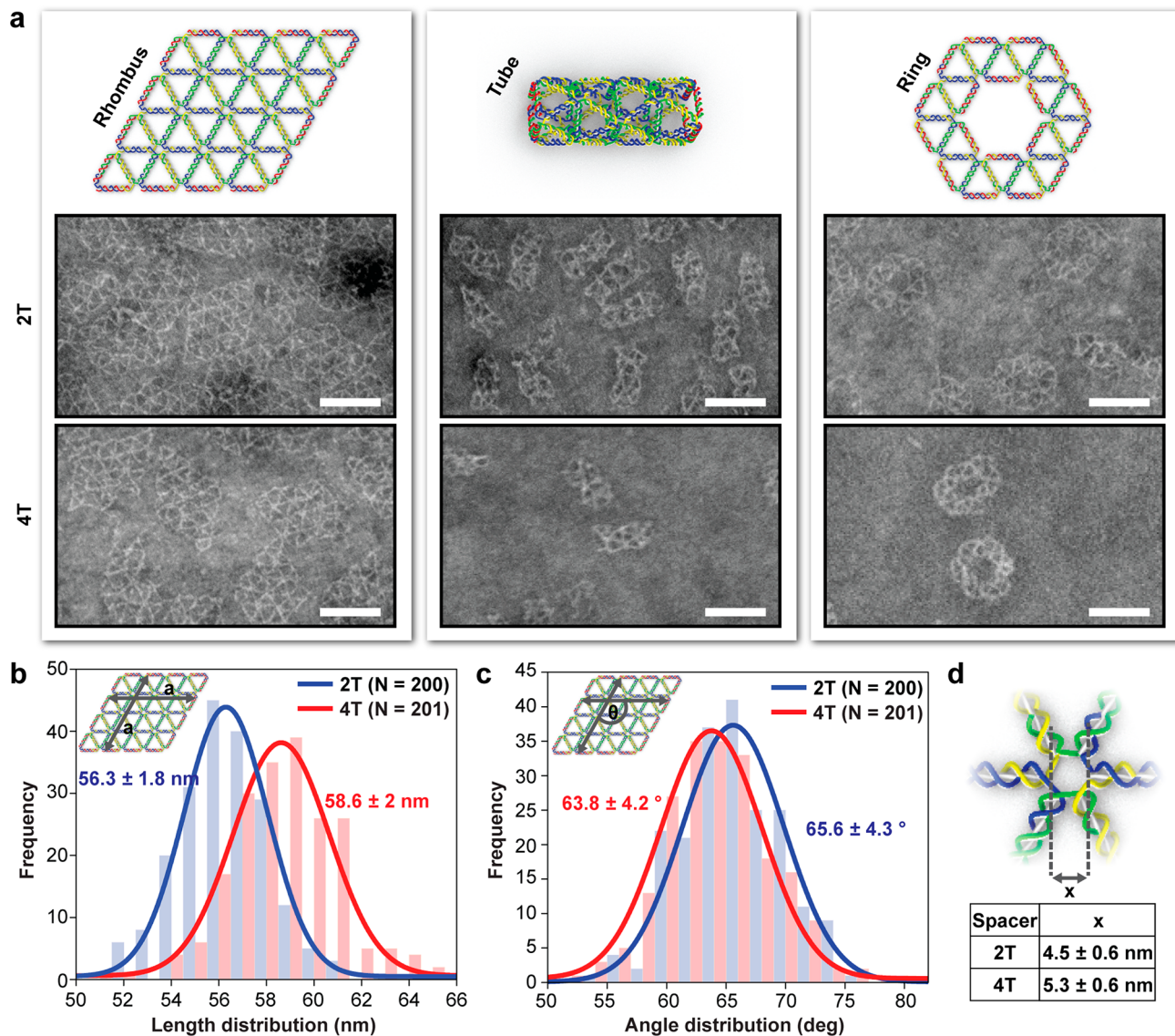


Figure 3. Structural analysis of the rhombus, tube, and ring structures. (a) 3D models and representative tSEM micrographs of the three finite test structures assembled with either a two- or four-thymine spacer (wide-field tSEM micrographs, Figures S7–S12). Scale bar: 50 nm. (b) Histogram of the structure width distribution and (c) the angular distribution of the rhombus structures measured along the sides (inset) for 2 nt (blue) and 4 nt (red) spacer structures (see Figures S13–S15 for measurement details). (d) Average six-arm junction gap width was calculated using the mean values of the width distribution.

our model, large structures contain many of such junctions, and during the assembly the likelihood of errors coming from nonplanar hybridization of new strands increases with the number of participating junctions. Therefore, we think that even small energy differences in individual junctions can affect the assembly yield because they will accumulate in a larger structure.

Based on these results, we further optimized the assembly process for structures having either two- or four-nucleotide spacer in the core strands. We designed three more test structures: a rhombus, a tube, and a ring. These structures were assembled at 12 mM MgCl₂ and a slow annealing ramp of 16 h (Figure 3a; wide-field tSEM micrographs Figures S7–S12). All structures form with good yield (Figure 1e). The 4 nt spacer introduction is particularly favorable for the rhombic and the ring structure, increasing the folding yield of the structures two times. For the tube structure, a smear is observed across the entire gel lane area for both the 2 and 4 nt spacer design,

indicating the formation of undesired multimer structures (distinct dimer and trimer bands can be observed; see Figure 1d).

To verify the geometry of the assembled structures, we calculated the ratio of two adjacent side widths of the rhombus structure on transmission electron micrographs using ImageJ (Figures S13 and S14). In agreement with a rhombus having all the sides of equal lengths, the assembled structures have the mean distribution of this ratio centered around one (Figure S15). From the histograms for the side length distribution from the same set of measurements, it can be observed that the 2 nt spacer structure on average has a smaller side length and is less flexible than the 4 nt spacer design (Figure 3b–d).

The yield of the structures containing a 4 nt spacer using MgCl₂ buffers was always slightly better than for the 2 nt spacer version (Figure S16). As opposed to compact 3-dimensional structures SSB structures,³⁵ which require high salt concentrations, the hollow wireframe structures fold even

in physiological salt concentrations. Maximal assembly yield is achieved when buffers containing ~300 mM NaCl are used (Figure S16). We attribute this to a reduced aggregation tendency of DNA structures with monovalent cations compared with divalent cations, as divalent cations are facilitating the formation of salt bridges between adjacent DNA structures.⁵⁸

In contrast to their DNA-origami counterparts presented previously,^{44,43,45,26} the triangulated SST structures assemble with higher yields in higher salinities (300 mM NaCl compared to ~150 mM). We hypothesize that a stronger stabilization by salts is necessary due to reduced cooperativity and the lack of the templating scaffold strand. Moreover, all domains are only 10 or 11 nt long, whereas most origami designs contain also longer domains. Nevertheless, structures are also stable at physiologically relevant conditions (Figure 4).

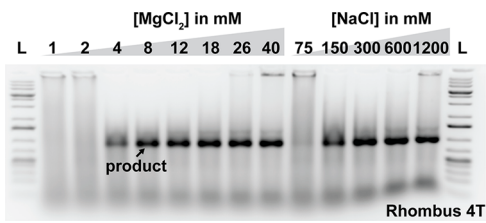


Figure 4. Fluorescence scan of the rhombus (4R4C) 4 spacer design after agarose gel electrophoresis (AGE) assembled in buffer containing different MgCl_2 or NaCl concentrations. The structures fold at physiological conditions (150 mM NaCl).

Extending folding times from 16 to 168 h did not improve the yield significantly (Figure S17). To further understand how the additional flexibility added by the spacer in the 6-arm junctions influences the flexibility of the rhombus, we simulated the assembled structure using the oxDNA model with a 0, 1, 2, and 4 nt long spacer (see the Materials and Methods section for details). The calculated mean structures of all designs show a preferential curvature (Figure 5), which is maximal for structures without the spacer. This indicates that breaking the stacking interactions may not be sufficient to assume a planar conformation and further supports the hypothesis of the accumulation of strain. The reduced global curvature for longer spacer sequences may also contribute to the higher assembly yield (Figure 1e).

1D SST Crystals. Another advantage of using SST structures is the ease of designing crystalline structures. Several design strategies have been explored, and among them, the tubular design is prominent.^{59,2} So far, nanotubes have been assembled from monomers with controllable circumferences, diameters, and stiffness.^{60–62,19,63} Furthermore, the activity of these monomers and other constituting components can also be controlled using cascade strand-displacement strategies.⁶⁴ The recent work of Schulman and colleagues demonstrates a similar approach in which the geometry of the nanotubes was controlled by introducing junction-seed structures to the assembly.⁶⁵ This approach allows to create higher-order two- or three-dimensional structures.

In this work, we also explored 1D SST crystals through making parts of the structure self-complementary (Figure 6a–c). The six-arm junction motif used for the assembly of the structures in this work is intrinsically flexible due to the spacer sequences. Therefore, the intramolecular tube formation is favored over the formation of flat ribbons (Figure 6d,e). As in

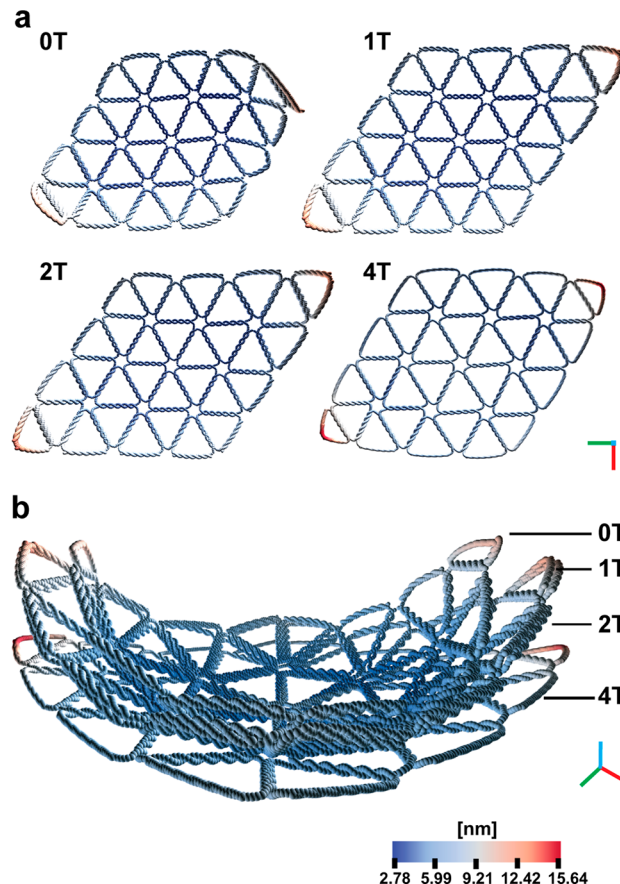


Figure 5. Coarse-grained molecular dynamics simulations using the oxDNA model of the rhombus structures with varying spacer lengths from 0 to 4 thymidine bases. (a) Top view of the mean rhombus structures with spacers ranging from 0 to 4 nt. The plotted structure shows the position of centers of mass of the average structure, obtained from averaging over 37 000 simulated states. Coloring corresponds to the mean deviation from the mean position for every base in the simulated structure. (b) Combined side view of the modeled structures showing distinct curvature. See trajectory animations 5–9 in the Supporting Information for representative trajectories of the simulated structures.

our previous work, we explore a number of possible connections of the basic ribbon.⁴⁵ Domain 1 (Figure 6a) can be made complementary to either domain A, B, C, or D, resulting in different tubes. Both four- and three-row designs were tested. For example, Figure 6d shows 3TB-4T, a 3-row tube, where domains 1 and B are made complementary and with a 4 nt spacer (Figures 6d and S5). In all cases, no distinct product band was observed on AGE other than a hanging lane at the pocket (Figure S18) indicating that most of the resulting reaction products are too large to enter the gel. tSEM micrographs reveal long tubes and a varying amount of undefined aggregates (Figures 6d,f, S19, and S32).

Interestingly, longer tubes were formed when the spacer length was 4 nt, with the longest tubes observed in the case of the 3TA structure, which corresponds to a tetrahedral truss (Figures 6g, S19, and S20). We hypothesize that compared with the 2 nt spacer, increasing the spacer to 4 nt decreased the strain in the structures, leading to a smaller energetic barrier for the polymerization interactions. However, flexibility of tubes with self-complementary ends can also lead to the formation of rings, which is entropically favorable due to the

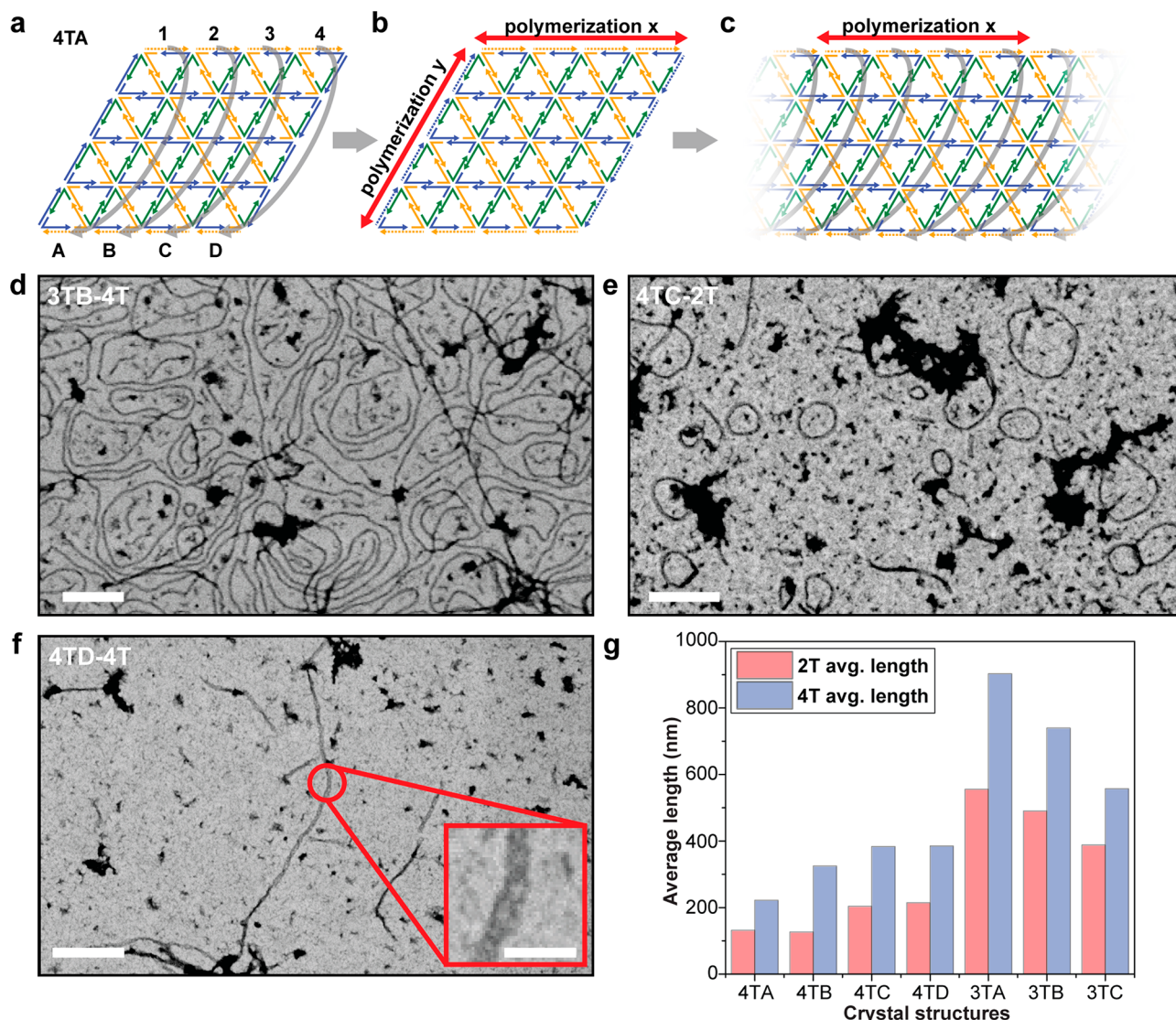


Figure 6. One-dimensional crystal formation using the triangulated SST approach. (a) As explained in more detail in Figure S5, the tube crystal name is composed of the number of triangle rows and the connectivity of the first top column of oligonucleotides. (b) Self-complementary edges lead to formation of an infinite 4TA crystal. (c) Because the six-arm junction used in the designs is flexible, once a complete column is formed, polymerization continues only in the lateral direction. The representative tSEM micrograph of the (d) 3TB structure with a 4 nt spacer, (e) 4TC structure with a 2 nt spacer, and (f) 4TD structure with a 4 nt spacer. Inset represents the zoomed-in version of the selected area in the red circle. The scale for all micrographs was 250 nm, and for the inset, it was 50 nm. (g) Summary of the observed average length of the tubular structures (at least 49 structures were taken for each measurement; for the exact numbers, see Figures S19–S32).

high local concentration of reactive ends. In our images, we also frequently observe ring formation. This additional flexibility is most likely also the reason for higher number of circularized tubes for the 4 nt spacer tube crystals (Figure S33).

Controlling the Crystal Size. Many of the observed tube crystal structures show a great amount of uncontrolled aggregates. To counter this problem, we were inspired by a recent approach proposed by Schulman and co-workers,⁶⁶ a seeded assembly approach to facilitating the controlled growth of the tubular crystals. As shown in Figure 7a, we introduced a long oligonucleotide complementary to one side of a 4TA tube crystal structure called “blocking strand”. It is unclear if the blocking strand acts as a crystallization seed, but in any case, effectively restricts the polymerization in one direction when incorporated into the tube crystal. Decreasing the concen-

tration of this blocking strands results in a gradual increase of the length of the main product. At a 1:1 ratio between the blocking strand and the oligonucleotides forming the 4TA tube crystal, mainly monomers (Figure 7c) and fewer dimers (Figure 7d) are formed. In a reaction with a 4:1 oligonucleotides to blocking strand ratio, octamer structures are observed as the leading product band (Figure 7h), indicating that it is possible to tune the length distributions of the formed tubes.

CONCLUSIONS

In this paper, we have extended the triangulated wireframe design strategy, previously only employed in DNA origami designs,^{26,44,45} to SST structures. For the design, we have developed an automated program (Hex-Tiles) that also assists the user in creating 96-well plate layouts for ordering, and

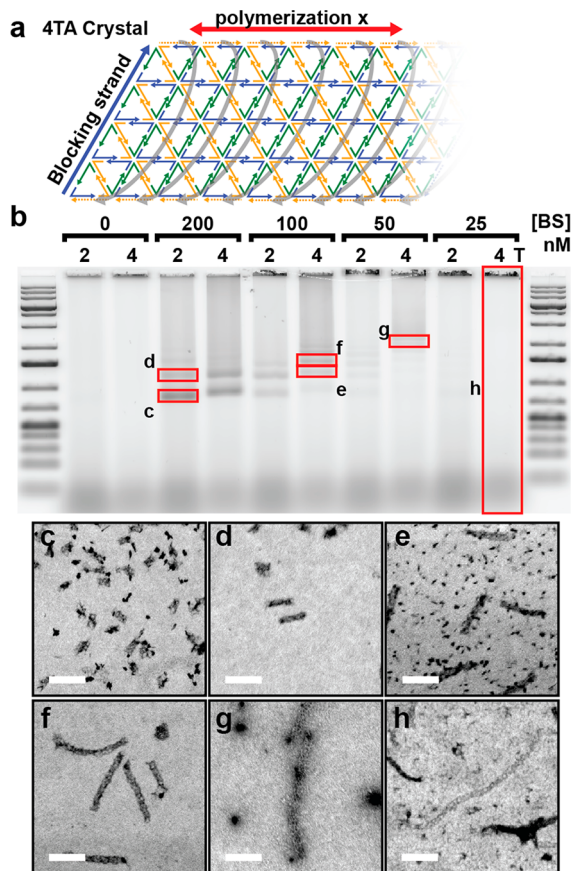


Figure 7. Controlling the crystal growth of 4TA structures using blocking strands. (a) The blocking strand is an oligonucleotide complementary to one of the sides of the 4TA crystal structure. (b) By controlling the concentration of the blocking strand, it is possible to shift the length distribution of the formed product. (c) Monomers, (d) dimers, (e) trimers, (f) tetramers, (g) octamers, and (h) long 1D crystals. Scale bar: 100 nm.

generating pipetting schemes to prepare oligonucleotide mixtures for the folding experiments. With this software, we designed and folded three finite structures: rhombus, tube and ring. We found that introducing spacers in the six-arm junctions connecting the double-stranded edges of the triangles is essential to fold the structures with good yields. The best assembly yield was observed for structures having a 4 nt thymidine spacer in a NaCl-containing buffer. Other than conventional DNA structures with close-packed helices, the triangulated wireframe structures form even under physiologically relevant salinities (150 mM NaCl), with better yields at 300 mM NaCl.

Coarse-grained molecular dynamics simulations of single six-arm junctions and rhombus structures imply that the absence of spacers in the six-arm junction motif leads to undesired stacking interactions and a strong global curvature of the structure. By designing domains on opposing sides of the rhombus to be complementary, several infinite tubular assemblies have been demonstrated. Further, we controlled the length distribution of the tubes by varying the concentration of a long blocking strand, complementary to one side of the rhombus.

The triangulated SST structures presented herein combine advantages of the scaffold-free single-stranded tile approach with those of triangulated hollow wireframe structures,

providing a cost-effective route for large-scale synthesis for nanomedical applications.

MATERIALS AND METHODS

SST Folding. For folding SST structures, the following mixture composition was used:

- (1) strands set (Integrated DNA Technologies or Eurofins) at 200 nM (each);
- (2) 1× folding buffer that consists of 300 mM NaCl, 10 mM Tris-HCl, adjusted to pH 7.9 and mixed; and

The mixture was annealed in a thermal cycler (Bio-Rad C1000 Touch) from 80 to 65 °C at a rate of $-1\text{ }^{\circ}\text{C}/\text{min}$ and from 65 °C to room temperature at a rate of $-1\text{ }^{\circ}\text{C}$ per 20 min, with excess oligonucleotides removed by agarose gel electrophoresis.

For the long folding reactions, the following variations were made to the annealing protocol:

- (1) 3 days protocol: 1 min at 80 °C, 80 to 60 °C at a rate of $-1\text{ }^{\circ}\text{C}/3\text{ min}$ and from 65 °C to room temperature at a rate of $-1\text{ }^{\circ}\text{C}$ per 2 h
- (2) 7 days protocol: 1 min at 80 °C followed by cooling down to 20 °C at the rate of $1\text{ }^{\circ}\text{C}/3\text{ h}$.

Following the annealing reaction, the samples were stored at 4 °C in 1.5 mL DNA LoBind vials (Eppendorf).

Agarose Gel Electrophoresis. For the AGE analysis, 1% agarose gels (DNA pure grade, VWR) were casted with 0.5× TBE buffer supplemented with 12 mM MgCl₂ and 1× Gelgreen nucleic acid gel stain (Biotium). TBE buffer (0.5×) with 12 mM MgCl₂ was used as a running buffer. A total of 15 μL of sample solution were mixed with 3 μL of 6× gel loading dye (50% glycerol, 5 mM Tris, 1 mM EDTA (at pH 8.0, 12 mM MgCl₂, 0.25% bromophenol blue, and 0.25% of xylene cyanol). Electrophoresis was performed at 70 V for 2 h at room temperature. As a reference, 10 μL of 1 kb plus DNA ladder (Thermo Scientific) were added. The gel was imaged with a Typhoon FLA 9500 gel scanner (GE Healthcare) using the excitation wavelength of 473 nm suitable for SYBR-safe stained gels.

For the purification of the SST structures, the desired band was cut out with a razor blade, and the excess agarose was carefully removed. The slice was then chopped, transferred into a DNA gel extraction column (Bio-Rad, Freeze'n Squeeze), and centrifuged at 4800 rcf, at room temperature for 5 min. After centrifugation, the inner filter tube was rotated by 180° and centrifuged again under same conditions to completely filter out the sample from the agarose debris. The purified sample was transferred into a DNA LoBind tube and stored at 4 °C.

tSEM Characterization. Carbon-coated TEM grids (400 mesh copper, carbon on Formvar, Science Services Munich) were plasma-treated for 15 s. A total of 5 μL of the sample solution was applied on the TEM grid and incubated for 3 min. The excess solution was removed from the grid with a filter paper. Next, 5 μL of a 2% uranyl formate solution was applied for 90 s to stain the DNA origami structures, and the solution was removed with a filter paper. The samples were scanned on Gemini SEM500 (Zeiss) operated at 30 kV using a transmission detector.

AFM Imaging. A total of 70 μL of a 0.01% poly-L-ornithine solution (Sigma-Aldrich) was placed on a piece of freshly cleaved mica. After 1 min, the mica surface was washed with water. A total of 3 μL of the respective sample were placed inside a circle (diameter ca. 3 mm) drawn with a permanent marker. After incubation for 1 min, 70 μL of 1× FB were added to the sample, and 30 μL of the same buffer was added onto the AFM tip (BioLever-mini, Olympus). Scanning was performed using AC liquid mode using a Cypher ES AFM (Asylum Research).

AGE-Based Folding-Yield Estimation. The quantification of the bands on AGE was done using ImageJ (<http://rsb.info.nih.gov/ij/>) according to the previously used technique.⁶⁷

Molecular Dynamics Simulations. The simulations of 6-arm junctions and rhombus structures were carried out using oxDNA2 version of the model with the sequence-dependent parametrization of hydrogen-bonding and stacking interactions.^{53,55} The simulations of

the single 6-arm junction (with 0, 1, 2, or 4 nt spacer between the arms) were carried out on CPUs using molecular dynamics (MD) simulation with an Andersen-like thermostat and simulation time step of 0.015 ps.⁶⁸ The temperature was set to 25 °C, and sodium concentration was set to 0.2 M using the Debye–Hückel model for electrostatic interactions. We ran the MD simulations for each of the junctions for number of steps time corresponding to 11 μs. A total of 40 replicas were run per junction. We note, however, that direct connection cannot be established between the time in the simulation and the corresponding time in experiment due to the highly coarse-grained nature of the model. Time scales of different processes (such as breaking of stacking interaction between bases or diffusion of the arms of junction) can scale with different ratios with respect to the actual time of the same process happening in experiment. Moreover, to speed up the sampling of different conformations of the junction, we are using diffusion coefficient that corresponds to $7.6 \times 10^{-8} \text{ m}^2/\text{s}$ of a 14 bp duplex in the simulation, which corresponds to approximately 600 times faster diffusion than observed experimentally.⁶⁹

The angles between arms were obtained by measuring the angle between helical axes of the respective arms. To obtain the helical axis, we connected the midpoints between second base pair (counting from the spacer) and the third consecutive base pair of the arms. The free-energy profiles in Figure 2 were obtained from the probability histogram of angles sampled by the system during the unbiased MD simulation (obtained by Boltzmann inversion). To verify that sufficient sampling of the angular space was reached, we plotted the free-energy profiles of the sampled states divided into three equal parts (Figure S34), we note that the standard deviation between the obtained plots is on the order of the plot line thickness. Thus, sufficient sampling was reached.

For the simulations of the rhombus structure, we use the GPU implementation of the MD code for oxDNA2⁷⁰ with a sodium concentration of 0.4 M, temperature of 30 °C, and simulation time step of 0.006 ps with a Langevin thermostat. Other parameters were the same as for the CPU simulation. We simulated each of the rhombus structures (with 0, 1, 2, and 4 nt spacer, respectively) for simulation time of 6 μs. A total of four replicas were performed per structure.

To obtain the average structure and calculate the mean deviation of position of each nucleotide, we saved 40 000 different conformations from the MD simulation on GPU (each saved after 600 ps). We then picked randomly one structure from the ensemble and aligned all of the remaining structures onto this one so that the root-mean-square distance between the centers of mass of all corresponding nucleotides is minimized. We then obtained the mean structure by averaging positions of center of mass of all nucleotides in the aligned ensemble. We verified that the obtained final mean structure is not sensitive to the choice of the randomly picked structure for the aligning and also found that the mean structure obtained is the same (within the standard deviation) if at least 6500 sampled states from the simulation are used to construct it, confirming that the simulation time was long enough to sample all relevant conformations.

ASSOCIATED CONTENT

Supporting Information

The Supporting Information is available free of charge on the ACS Publications website at DOI: [10.1021/acsnano.8b08009](https://doi.org/10.1021/acsnano.8b08009).

Animations trajectory_1-4 correspond to simulated states of the six-arm junctions with 0 to 4 nt spacers covering a time period of 30 ns. Duration between the frames corresponds to 151 ps. The frame rate is 1 fps. Animations trajectory_5-4 correspond to simulated states of the rhombus structure with 0 to 4 nt spacers covering a time period of 30 ns. Duration between the frames corresponds to 606 ps. The frame rate is 1 fps. Animation trajectory_9 corresponds to simulated states of the rhombus structure with a 2 nt spacer covering a

time period of 6 ns. Duration between the frames corresponds to 4 ps. The frame rate is 30 fps. ([ZIP](#)) Figures showing experimental, analysis, and calculation details and tSEM and AFM images ([PDF](#))

AUTHOR INFORMATION

Corresponding Authors

*E-mail: psulc@asu.edu.

*E-mail: Dr.T.L.Schmidt@gmail.com.

ORCID

Michael Matthies: [0000-0001-5979-1757](#)

Thorsten L. Schmidt: [0000-0002-6798-5241](#)

Present Address

¹Physics department, 103 Smith Hall, Kent State University, 44242 Kent, Ohio, United States

Author Contributions

M.M., F.M.J. and T.L.S. conceived the study, M.M. and F.M.J. wrote HexTiles and designed the structures, and M.M. and N.P.A. performed the experiments. N.P.A. performed the TEM measurements and M.M. performed the AFM imaging. Simulations were performed by M.M., E.P., and P.Š. M.M. and N.P.A wrote the manuscript and prepared the figures.

Notes

The authors declare no competing financial interest.

ACKNOWLEDGMENTS

We acknowledge the use of the imaging facilities in the Dresden Center for Nanoanalysis(DCN) and skillful advice from Dr. Markus Löffler as well as access to the AFM of Prof. Michael Mertig. We also acknowledge Anne Schulze for her administrative assistance. This work was funded by the DFG through the Center for Advancing Electronics Dresden (cfaed). Part of the simulations work used the Extreme Science and Engineering Discovery Environment (XSEDE),⁷¹ which is supported by National Science Foundation grant number ACI-154856 through allocation MCB180033. P.Š. further acknowledges the donation of GPU cards from the NVIDIA Corporation.

REFERENCES

- (1) Hong, F.; Zhang, F.; Liu, Y.; Yan, H. DNA Origami: Scaffolds for Creating Higher Order Structures. *Chem. Rev.* **2017**, *117*, 12584–12640.
- (2) Seeman, N. C.; Sleiman, H. F. DNA Nanotechnology. *Nat. Rev. Mater.* **2017**, *3*, 17068.
- (3) Ackermann, D.; Schmidt, T. L.; Hannam, J. S.; Purohit, C. S.; Heckel, A.; Famulok, M. A Double-Stranded DNA Rotaxane. *Nat. Nanotechnol.* **2010**, *5*, 436–442.
- (4) Schmidt, T. L.; Heckel, A. Construction of a Structurally Defined Double-Stranded DNA Catenane. *Nano Lett.* **2011**, *11*, 1739–1742.
- (5) Lu, C.-H.; Cecconello, A.; Qi, X.-J.; Wu, N.; Jester, S.-S.; Famulok, M.; Matthies, M.; Schmidt, T.-L.; Willner, I. Switchable Reconfiguration of a Seven-Ring Interlocked DNA Catenane Nanostructure. *Nano Lett.* **2015**, *15*, 7133–7137.
- (6) Kuzyk, A.; Jungmann, R.; Acuna, G. P.; Liu, N. DNA Origami Route for Nanophotonics. *ACS Photonics* **2018**, *5*, 1151–1163.
- (7) Gür, F. N.; Schwarz, F. W.; Ye, J.; Diez, S.; Schmidt, T. L. Toward Self-Assembled Plasmonic Devices: High-Yield Arrangement of Gold Nanoparticles on DNA Origami Templates. *ACS Nano* **2016**, *10*, 5374–5382.
- (8) Gür, F. N.; McPolin, C. P. T.; Raza, S.; Mayer, M.; Roth, D. J.; Steiner, A. M.; Löffler, M.; Fery, A.; Brongersma, M. L.; Zayats, A. V.; König, T. A. F.; Schmidt, T. L. DNA-Assembled Plasmonic

- Waveguides for Nanoscale Light Propagation to a Fluorescent Nanodiamond. *Nano Lett.* **2018**, *18*, 7323–7329.
- (9) Castro, C. E.; Dietz, H.; Höglberg, B. DNA Origami Devices for Molecular-Scale Precision Measurements. *MRS Bull.* **2017**, *42*, 925–929.
- (10) Nickels, P. C.; Wünsch, B.; Holzmeister, P.; Bae, W.; Kneer, L. M.; Grohmann, D.; Tinnefeld, P.; Liedl, T. Molecular Force Spectroscopy with a DNA Origami-Based Nanoscopic Force Clamp. *Science* **2016**, *354*, 305–307.
- (11) Kilchherr, F.; Wachauf, C.; Pelz, B.; Rief, M.; Zacharias, M.; Dietz, H. Single-Molecule Dissection of Stacking Forces in DNA. *Science* **2016**, *353*, aaf5508.
- (12) Zheng, J.; Birktoft, J. J.; Chen, Y.; Wang, T.; Sha, R.; Constantinou, P. E.; Ginell, S. L.; Mao, C.; Seeman, N. C. From Molecular to Macroscopic via the Rational Design of a Self-Assembled 3D DNA Crystal. *Nature* **2009**, *461*, 74–77.
- (13) Martin, T. G.; Bharat, T. A. M.; Joerger, A. C.; Bai, X.; Praetorius, F.; Fersht, A. R.; Dietz, H.; Scheres, S. H. W. Design of a Molecular Support for Cryo-EM Structure Determination. *Proc. Natl. Acad. Sci. U. S. A.* **2016**, *113*, E7456–E7463.
- (14) Zhang, T.; Hartl, C.; Frank, K.; Heuer-Jungemann, A.; Fischer, S.; Nickels, P. C.; Nickel, B.; Liedl, T. 3D DNA Origami Crystals. *Adv. Mater.* **2018**, *30*, 1800273.
- (15) Chakraborty, K.; Veetil, A. T.; Jaffrey, S. R.; Krishnan, Y. Nucleic Acid-Based Nanodevices in Biological Imaging. *Annu. Rev. Biochem.* **2016**, *85*, 349–373.
- (16) Okholm, A. H.; Kjems, J. The Utility of DNA Nanostructures for Drug Delivery *in Vivo*. *Expert Opin. Drug Delivery* **2017**, *14*, 137–139.
- (17) Rothemund, P. W. K. Folding DNA to Create Nanoscale Shapes and Patterns. *Nature* **2006**, *440*, 297–302.
- (18) Douglas, S. M.; Dietz, H.; Liedl, T.; Höglberg, B.; Graf, F.; Shih, W. M. Self-Assembly of DNA into Nanoscale Three-Dimensional Shapes. *Nature* **2009**, *459*, 414–418.
- (19) Yin, P.; Hariadi, R. F.; Sahu, S.; Choi, H. M. T.; Park, S. H.; LaBean, T. H.; Reif, J. H. Programming DNA Tube Circumferences. *Science* **2008**, *321*, 824–826.
- (20) Wei, B.; Dai, M.; Yin, P. Complex Shapes Self-Assembled from Single-Stranded DNA Tiles. *Nature* **2012**, *485*, 623–626.
- (21) Ke, Y.; Ong, L. L.; Shih, W. M.; Yin, P. Three-Dimensional Structures Self-Assembled from DNA Bricks. *Science* **2012**, *338*, 1177–1183.
- (22) Hong, F.; Zhang, F.; Liu, Y.; Yan, H. DNA Origami: Scaffolds for Creating Higher Order Structures. *Chem. Rev.* **2017**, *117*, 12584–12640.
- (23) Douglas, S. M.; Marblestone, A. H.; Teerapittayanon, S.; Vazquez, A.; Church, G. M.; Shih, W. M. Rapid Prototyping of 3D DNA-Origami Shapes with CaDNAno. *Nucleic Acids Res.* **2009**, *37*, 5001–5006.
- (24) Wei, B.; Dai, M.; Myhrvold, C.; Ke, Y.; Jungmann, R.; Yin, P. Design Space for Complex DNA Structures. *J. Am. Chem. Soc.* **2013**, *135*, 18080–18088.
- (25) Dunn, K. E.; Dannenberg, F.; Ouldridge, T. E.; Kwiatkowska, M.; Turberfield, A. J.; Bath, J. Guiding the Folding Pathway of DNA Origami. *Nature* **2015**, *525*, 82–86.
- (26) Agarwal, N. P.; Matthies, M.; Joffroy, B.; Schmidt, T. L. Structural Transformation of Wireframe DNA Origami *via* DNA Polymerase Assisted Gap-Filling. *ACS Nano* **2018**, *12*, 2546–2553.
- (27) Praetorius, F.; Kick, B.; Behler, K. L.; Honemann, M. N.; Weuster-Botz, D.; Dietz, H. Biotechnological Mass Production of DNA Origami. *Nature* **2017**, *552*, 84.
- (28) Ong, L. L.; Hanikel, N.; Yaghi, O. K.; Grun, C.; Strauss, M. T.; Bron, P.; Lai-Kee-Him, J.; Schueder, F.; Wang, B.; Wang, P.; Kishi, J. Y.; Myhrvold, C.; Zhu, A.; Jungmann, R.; Bellot, G.; Ke, Y.; Yin, P. Programmable Self-Assembly of Three-Dimensional Nanostructures from 10,000 Unique Components. *Nature* **2017**, *552*, 72.
- (29) Kocabey, S.; Meini, H.; MacPherson, I. S.; Cassinelli, V.; Manetto, A.; Rothenfusser, S.; Liedl, T.; Lichtenegger, F. S. Cellular Uptake of Tile-Assembled DNA Nanotubes. *Nanomaterials* **2015**, *5*, 47–60.
- (30) Sellner, S.; Kocabey, S.; Nekolla, K.; Krombach, F.; Liedl, T.; Rehberg, M. DNA Nanotubes as Intracellular Delivery Vehicles *in Vivo*. *Biomaterials* **2015**, *53*, 453–463.
- (31) Cassinelli, V.; Oberleitner, B.; Sobotta, J.; Nickels, P.; Grossi, G.; Kempfer, S.; Frischmuth, T.; Liedl, T.; Manetto, A. One-Step Formation of “Chain-Armor”-Stabilized DNA Nanostructures. *Angew. Chem., Int. Ed.* **2015**, *54*, 7795–7798.
- (32) Hahn, J.; Wickham, S. F. J.; Shih, W. M.; Perrault, S. D. Addressing the Instability of DNA Nanostructures in Tissue Culture. *ACS Nano* **2014**, *8*, 8765–8775.
- (33) Agarwal, N. P.; Matthies, M.; Gür, F. N.; Osada, K.; Schmidt, T. L. Block Copolymer Micellization as a Protection Strategy for DNA Origami. *Angew. Chem., Int. Ed.* **2017**, *56*, 5460–5464.
- (34) Ponnuswamy, N.; Bastings, M. M. C.; Nathwani, B.; Ryu, J. H.; Chou, L. Y. T.; Vinther, M.; Li, W. A.; Anastassacos, F. M.; Mooney, D. J.; Shih, W. M. Oligolysine-Based Coating Protects DNA Nanostructures from Low-Salt Denaturation and Nuclease Degradation. *Nat. Commun.* **2017**, *8*, 15654.
- (35) Ke, Y.; Ong, L. L.; Sun, W.; Song, J.; Dong, M.; Shih, W. M.; Yin, P. DNA Brick Crystals with Prescribed Depths. *Nat. Chem.* **2014**, *6*, 994–1002.
- (36) Schiffels, D.; Liedl, T.; Fygenson, D. K. Nanoscale Structure and Microscale Stiffness of DNA Nanotubes. *ACS Nano* **2013**, *7*, 6700–6710.
- (37) Schnauß, J.; Glaser, M.; Lorenz, J. S.; Schuldt, C.; Möser, C.; Sajfutdinow, M.; Händler, T.; Käs, J. A.; Smith, D. M. DNA Nanotubes as a Versatile Tool to Study Semiflexible Polymers. *J. Visualized Exp.* **2017**, *128*, e56056–e56056.
- (38) Schuldt, C.; Schnauß, J.; Händler, T.; Glaser, M.; Lorenz, J.; Golde, T.; Käs, J. A.; Smith, D. M. Tuning Synthetic Semiflexible Networks by Bending Stiffness. *Phys. Rev. Lett.* **2016**, *117*, 197801.
- (39) Maier, A. M.; Weig, C.; Oswald, P.; Frey, E.; Fischer, P.; Liedl, T. Magnetic Propulsion of Microswimmers with DNA-Based Flagellar Bundles. *Nano Lett.* **2016**, *16*, 906–910.
- (40) Castro, C. E.; Su, H.-J.; Marras, A. E.; Zhou, L.; Johnson, J. Mechanical Design of DNA Nanostructures. *Nanoscale* **2015**, *7*, 5913–5921.
- (41) Han, D.; Pal, S.; Yang, Y.; Jiang, S.; Nangreave, J.; Liu, Y.; Yan, H. DNA Gridiron Nanostructures Based on Four-Arm Junctions. *Science* **2013**, *339*, 1412–1415.
- (42) Simmel, S. S.; Nickels, P. C.; Liedl, T. Wireframe and Tensegrity DNA Nanostructures. *Acc. Chem. Res.* **2014**, *47*, 1691–1699.
- (43) Zhang, F.; Jiang, S.; Wu, S.; Li, Y.; Mao, C.; Liu, Y.; Yan, H. Complex Wireframe DNA Origami Nanostructures with Multi-Arm Junction Vertices. *Nat. Nanotechnol.* **2015**, *10*, 779–784.
- (44) Benson, E.; Mohammed, A.; Gardell, J.; Masich, S.; Czeizler, E.; Orponen, P.; Höglberg, B. DNA Rendering of Polyhedral Meshes at the Nanoscale. *Nature* **2015**, *523*, 441–444.
- (45) Matthies, M.; Agarwal, N. P.; Schmidt, T. L. Design and Synthesis of Triangulated DNA Origami Trusses. *Nano Lett.* **2016**, *16*, 2108–2113.
- (46) Benson, E.; Mohammed, A.; Bosco, A.; Teixeira, A. I.; Orponen, P.; Höglberg, B. Computer-Aided Production of Scaffolded DNA Nanostructures from Flat Sheet Meshes. *Angew. Chem., Int. Ed.* **2016**, *55*, 8869–8872.
- (47) Veneziano, R.; Ratanalert, S.; Zhang, K.; Zhang, F.; Yan, H.; Chiu, W.; Bathe, M. Designer Nanoscale DNA Assemblies Programmed from the Top Down. *Science* **2016**, *352*, 1534–1534.
- (48) Hong, F.; Jiang, S.; Wang, T.; Liu, Y.; Yan, H. 3D Framework DNA Origami with Layered Crossovers. *Angew. Chem.* **2016**, *128*, 13024–13027.
- (49) Williams, S.; Lund, K.; Lin, C.; Wonka, P.; Lindsay, S.; Yan, H. Tiamat.: A Three-Dimensional Editing Tool for Complex DNA Structures. In *DNA Computing*; Goel, A., Simmel, F. C., Sosik, P., Eds.; Lecture Notes in Computer Science; Springer Berlin Heidelberg: Berlin, Germany, 2009; pp 90–101.

- (50) Zhu, J.; Wei, B.; Yuan, Y.; Mi, Y. UNIQUIMER 3D, a Software System for Structural DNA Nanotechnology Design, Analysis and Evaluation. *Nucleic Acids Res.* **2009**, *37*, 2164–2175.
- (51) Wang, Y.; Mueller, J. E.; Kemper, B.; Seeman, N. C. Assembly and Characterization of Five-Arm and Six-Arm DNA Branched Junctions. *Biochemistry* **1991**, *30*, 5667–5674.
- (52) Ouldridge, T. E.; Louis, A. A.; Doye, J. P. K. Structural, Mechanical, and Thermodynamic Properties of a Coarse-Grained DNA Model. *J. Chem. Phys.* **2011**, *134*, 085101.
- (53) Šulc, P.; Romano, F.; Ouldridge, T. E.; Rovigatti, L.; Doye, J. P. K.; Louis, A. A. Sequence-Dependent Thermodynamics of a Coarse-Grained DNA Model. *J. Chem. Phys.* **2012**, *137*, 135101.
- (54) Snodin, B. E. K.; Randisi, F.; Mosayebi, M.; Šulc, P.; Schreck, J. S.; Romano, F.; Ouldridge, T. E.; Tsukanov, R.; Nir, E.; Louis, A. A.; Doye, J. P. K. Introducing Improved Structural Properties and Salt Dependence into a Coarse-Grained Model of DNA. *J. Chem. Phys.* **2015**, *142*, 234901.
- (55) Doye, J. P. K.; Ouldridge, T. E.; Louis, A. A.; Romano, F.; Šulc, P.; Matek, C.; Snodin, B. E. K.; Rovigatti, L.; Schreck, J. S.; Harrison, R. M.; Smith, W. P. J. Coarse-Graining DNA for Simulations of DNA Nanotechnology. *Phys. Chem. Chem. Phys.* **2013**, *15*, 20395–20414.
- (56) Kočar, V.; Schreck, J. S.; Čeru, S.; Gradišar, H.; Bašić, N.; Pisanski, T.; Doye, J. P. K.; Jerala, R. Design Principles for Rapid Folding of Knotted DNA Nanostructures. *Nat. Commun.* **2016**, *7*, 10803.
- (57) Engel, M. C.; Smith, D. M.; Jobst, M. A.; Sajfutdinow, M.; Liedl, T.; Romano, F.; Rovigatti, L.; Louis, A. A.; Doye, J. P. K. Force-Induced Unravelling of DNA Origami. *ACS Nano* **2018**, *12*, 6734–6747.
- (58) Luan, B.; Aksimentiev, A. DNA Attraction in Monovalent and Divalent Electrolytes. *J. Am. Chem. Soc.* **2008**, *130*, 15754–15755.
- (59) Glaser, M.; Schnauß, J.; Tscherner, T.; Schmidt, B. U. S.; Moebius-Winkler, M.; Käs, J. A.; Smith, D. M. Self-Assembly of Hierarchically Ordered Structures in DNA Nanotube Systems. *New J. Phys.* **2016**, *18*, 055001.
- (60) Rothmund, P. W. K.; Ekani-Nkodo, A.; Papadakis, N.; Kumar, A.; Fygenson, D. K.; Winfree, E. Design and Characterization of Programmable DNA Nanotubes. *J. Am. Chem. Soc.* **2004**, *126*, 16344–16352.
- (61) Aldaye, F. A.; Lo, P. K.; Karam, P.; McLaughlin, C. K.; Cosa, G.; Sleiman, H. F. Modular Construction of DNA Nanotubes of Tunable Geometry and Single- or Double-Stranded Character. *Nat. Nanotechnol.* **2009**, *4*, 349–352.
- (62) Hou, S.; Wang, J.; Martin, C. R. Template-Synthesized DNA Nanotubes. *J. Am. Chem. Soc.* **2005**, *127*, 8586–8587.
- (63) Wilner, O. I.; Orbach, R.; Henning, A.; Teller, C.; Yehezkel, O.; Mertig, M.; Harries, D.; Willner, I. Self-Assembly of DNA Nanotubes with Controllable Diameters. *Nat. Commun.* **2011**, *2*, 540.
- (64) Zhang, D. Y.; Hariadi, R. F.; Choi, H. M. T.; Winfree, E. Integrating DNA Strand-Displacement Circuitry with DNA Tile Self-Assembly. *Nat. Commun.* **2013**, *4*, 1965.
- (65) Jorgenson, T. D.; Mohammed, A. M.; Agrawal, D. K.; Schulman, R. Self-Assembly of Hierarchical DNA Nanotube Architectures with Well-Defined Geometries. *ACS Nano* **2017**, *11*, 1927–1936.
- (66) Mohammed, A. M.; Schulman, R. Directing Self-Assembly of DNA Nanotubes Using Programmable Seeds. *Nano Lett.* **2013**, *13*, 4006–4013.
- (67) Douglas, S. M. Rapid Prototyping of 3D DNA-Origami Shapes with CaDNAno. *Nucleic Acids Res.* **2009**, *37*, 5001–5006.
- (68) Russo, J.; Tartaglia, P.; Sciortino, F. Reversible Gels of Patchy Particles: Role of the Valence. *J. Chem. Phys.* **2009**, *131*, 014504.
- (69) Lapham, J.; Rife, J. P.; Moore, P. B.; Crothers, D. M. Measurement of Diffusion Constants for Nucleic Acids by NMR. *J. Biomol. NMR* **1997**, *10*, 255–262.
- (70) Rovigatti, L.; Šulc, P.; Reguly, I. Z.; Romano, F. A Comparison between Parallelization Approaches in Molecular Dynamics Simulations on GPUs. *J. Comput. Chem.* **2015**, *36*, 1–8.
- (71) Towns, J.; Cockerill, T.; Dahan, M.; Foster, I.; Gaither, K.; Grimshaw, A.; Hazlewood, V.; Lathrop, S.; Lifka, D.; Peterson, G. D.; Roskies, R.; Scott, J. R.; Wilkins-Diehr, N. XSEDE: Accelerating Scientific Discovery. *Comput. Sci. Eng.* **2014**, *16*, 62–74.